https://doi.org/10.1016/j.jmmm.2021.167943

Prediction of fatigue damage in ribbed steel bars under cyclic loading with a magneto-mechanical coupling model

Dawei Zhang[a]*, Wenqiang Huang[a], Jun Zhang[b], Weiliang Jin[a] and You Dong[c]

[a]*Institute of Structural Engineering, ZheJiang University, Hangzhou 310058, China*

[b]*Ningbo Tech University, Ningbo 315100, China*

[c]*Department of Civil and Environmental Engineering, Hong Kong Polytechnic University, Hong Kong 999077, China*

Abstract: As a ferromagnetic material, the magnetization of ribbed steel bars will change with the development of fatigue damage under cyclic loading, which can be used to evaluate the fatigue damage state of steel bars. However, the quantitative relationship between fatigue damage and the variation in magnetization is still unclear, and the existing magneto-mechanical model cannot be applied to ribbed steel bars directly. To accurately predict the magnetization and the fatigue damage state during fatigue, it is also necessary to consider the influence of stress concentration caused by ribs on stress and fatigue life. This paper proposes a magneto-mechanical model suitable for ribbed steel bars, which use the Neuber law and Coffin-Manson relationship to determine the stress range and fatigue life under stress concentration. Additionally, the magnetic induction intensity of the HRB400 ribbed steel bar in the tensile fatigue test was measured to verify the proposed model, and the mechanism of the magnetization change trend during fatigue was analyzed in detail. Through the fatigue damage formula based on the magnetic indicator, the simulation and experimental comparison results show that the proposed model can effectively describe the fatigue damage state of ribbed steel bars in the fatigue.

Keywords: Cyclic loads; fatigue damage; magneto-mechanical effect; ribbed steel bar.

1. Introduction

With the development and application of high-strength building materials, and the probability limit state design method based on reliability theory and concrete multi-axis strength theory is widely used in practical engineering design. The safety of the reinforced concrete (RC) structures under static load has been greatly guaranteed, they are difficult to destroy since they exceed their ultimate bearing capacity. More attention should be paid to the impact of long-term structural performance, one of the key points is the fatigue which causes the degradation of material mechanical properties. The structure is not only subjected to static load, but also often subjected to cyclic loads, such as earthquakes, wind loads, and vehicle loads, lower than the ultimate load during service. These loads usually cause the bars in the RC structure to develop fatigue cracks and irreversible damage to the local microstructure. When a particular critical value of damage is reached, the bars will undergo brittle fatigue fracturing, which causes RC structure failure [1]. Therefore, accurate evaluations of fatigue damage to steel bars are an essential means to ensuring structural safety and reliability. Currently, the research methods for assessing the fatigue of materials include S-N curves, fracture mechanics and damage mechanics. These methods are mainly based on traditional mechanical indicators to analyze the fatigue properties of materials [2]. However, the variation in the stress-strain hysteresis curve of steel bars during fatigue is slight and monotonous, which makes it difficult to reflect the microscopic damage and accurately evaluate the fatigue damage state. Additionally, strain measuring equipment needs to be installed inside the structure, and regular maintenance and replacement are required to ensure long-term effectiveness. These factors result in damage to the structure and high costs.

There are certain limitations to using traditional mechanical indicators to reflect the material fatigue damage. In recent years, spontaneous magnetic field (SMF) technology, which has been used to estimate the damage of ferromagnetic materials by detecting the change in the weak magnetic signal on the surface of the materials, is considered to be of great feasibility for applications in fatigue damage detection involving ferromagnetic materials [3]. As a ferromagnetic material, the magnetization properties of ribbed steel bars are very sensitive to the stress loading history and fatigue microscopic damage [4]. Villari [5] first systematically studied the magnetic behavior of ferromagnetic materials under an external magnetic field and stress. The study showed that the magnetic domains within materials would move and rotate under a monotone loading, leading to changes in the surface magnetic field of the material. Erber et al. [6] found that the surface magnetic signals of ferromagnetic materials under cyclic loading reflect internal dislocation slippage due to the accumulated microplasticity of fatigue. Guralnick et al. [7] measured the magnetic induction intensity of AISI 1080 steel under tensile and compressive fatigue tests. They found that the magnetic hysteresis curve of specimens contained more information about fatigue damage, and the area of the magnetic hysteresis curve changed in three stages with the development of fatigue damage. Subsequently, Bao et al. [8-11] also conducted similar fatigue test research, which showed that the magnetic hysteresis curve could more sensitively reflect the microstructure damage than the corresponding mechanical hysteresis curve. In torsion and bending fatigue, the variations in magnetic signals also show regularity [12]. Xu et al. found that the magnetic signal in medium carbon steel in a rotational bending fatigue test showed a systematic three-stage trend: a rapid increase in the early stage, a stable development in the middle stage, and a sudden change in the final stage. To verify the feasibility of SMF application on ribbed steel bars, Zhang et al. [4] measured the surface magnetic induction of ribbed steel bars in tensile fatigue tests and reflected the fatigue damage state of the bars by the change rate in the magnetic induction. Current experimental studies have proven that the magnetization property and SMF of ferromagnetic materials have the potential to be used as detection indicators for fatigue damage. However, most of them are still in a state of qualitative research. To accurately evaluate the fatigue damage stage of ferromagnetic materials, a theoretical model to quantitatively describe the magnetization of ferromagnetic materials during fatigue is indispensable.

The magnetization and SMF of ferromagnetic materials are mainly related to the magneto-mechanical effect during fatigue. Jiles and Atherton [13-15] proposed a phenomenological model (J-A model) for ferromagnetic materials to characterize the relationship between stress and magnetization, which has been widely used in studying the magnetic behavior of ferromagnetic materials under stress. In the actual magnetization process, dislocations and domain wall pinning will affect the magnetic properties of the material. Sablik et al. [16-18] introduced pinning coefficients into the J-A model and established the Jiles-Atherton-Sablik (J-A-S) hysteresis model. Then, Li et al. [19] took the influence of plastic deformation on magnetization into account and modified the plastic term of the J-A-S model. To facilitate calculating the fatigue, Xu et al. [20] proposed the magnetization local equilibrium state based on dislocation magnetization theory and established a relationship between the fatigue damage and magnetization by the modified J-A-S model. On the other hand, Zheng and Liu [21] established the Zheng-Liu (Z-L) model using thermodynamic relations, which can predict a magnetostrictive strain under different magnetic fields with different pre-pressures. Based on the Z-L model and combined with the approach law, Shi et al. [22] made the model more accurate in describing the magnetization under a few cyclic loads, but it did not consider the effect of fatigue damage on the magnetization property of the material. Recently, Huang et al. [23] combined the Z-L model and the modified J-A-S model based on the plastic strain obtained from the test and simulated the magnetization of smooth specimens processed by HRB400 steel bars during fatigue. However, the fatigue model and the simulation of ribbed steel bars remain to be studied.

In general, most of the existing magneto-mechanical fatigue models are suitable for smooth and homogeneous specimens, but the ribbed bars in RC structures are not smooth and homogeneous materials. Their ribs on the surface will significantly affect the stress distribution, and these stresses are closely related to fatigue life and magnetization. In addition, the simulation results of the existing models depend on the plastic strain measured during each cycle. If theoretical analysis or data regression can be used to make them independent of the test data, it will bring great convenience to the simulation. To accurately predict the magnetization evolution of ribbed steel bars in RC structures during fatigue under complex fatigue stress, the fatigue model of ribbed bars will provide reference and guidance. In this paper, based on the model established by Huang et al. [23], the influence of the stress concentration is considered in order to determine the simulated stress range and fatigue life, and the residual plastic strain formula of ribbed steel bars conforming to the three-stage development law is combined to establish a fatigue magneto-mechanical model applicable to ribbed steel bars. In addition, tensile fatigue tests of HRB400 ribbed steel bars are performed, and the simulation results of the modified model are compared with the test results to verify the applicability and accuracy.

2. Magneto-mechanical theoretical framework

2.1.Magneto-mechanical model under ideal magnetization

If the influence of the stress loading history on the magnetization of ferromagnetic materials is ignored, the materials will ideally be magnetized in the magnetic field, and their magnetization will tend to be anhysteretic. In addition, ferromagnetic materials subjected to stress will produce magnetostrictive strain, which manifests the displacement and rotation of the domain walls. In this process, part of the stress energy will be converted into magnetization energy, and the macroscopic magnetization eventually changes.

Because the ribbed steel bar's axial dimension is much larger than its radial dimension, it can be regarded as a one-dimensional isotropic ferromagnetic rod. Under the isothermal environment and a constant axial weak magnetic field, ignoring the loading history, the total derivative of energy per unit volume of material satisfies the following equation [24]:

$$\mathrm{d}U = \sigma \mathrm{d}\varepsilon + T\mathrm{d}S + \mu_0 (H - N_d M)\mathrm{d}M \quad (1)$$

where σ is the stress, ε is the strain, T is the temperature, S is the entropy density, $\mu_0 = 4\pi \times 10^{-7}$A/m is the vacuum permeability, H is the magnetic field strength, N_d is the demagnetization coefficient, and M is the magnetization.

The Gibbs free energy of ferromagnetic materials during magnetization can be expressed as [25]

$$G(\sigma, M, T) = U - TS - \sigma\varepsilon \tag{2}$$

For the isothermal case, $SdT = 0$, the following thermodynamic relations can be obtained.

$$\varepsilon = -\frac{\partial G}{\partial \sigma}, \mu_0(H - N_d M) = \frac{\partial G}{\partial M} \tag{3}$$

Use independent variables to extend the Gibbs free energy function at $G(\sigma, M) = G(0,0)$, and substitute the expanded Taylor series into equation (3) to obtain the polynomial expression of the effective magnetic field H_e with stress σ and magnetization M. Combined with the theoretical analysis of Jiles et al. [13], the magnetostriction curve of the ferromagnetic materials is a symmetrical even function, so that the one-dimensional magneto-mechanical constitutive relationship can be expressed as [23]:

$$H_e = \begin{cases} H_0 + \alpha M - N_d M + \frac{2\lambda_s M}{\mu_0 M_\mathrm{ws}^2}\left(\sigma - \frac{\sigma_s}{\beta}\text{In}\cosh\frac{\beta\sigma}{\sigma_s}\right) - \frac{4\theta\lambda_s\sigma\left(M^3 - M_r^3(\sigma)\right)}{\mu_0 M_\mathrm{ws}^4}, \sigma \geq 0 \\ H_0 + \alpha M - N_d M + \frac{2\lambda_s M}{\mu_0 M_\mathrm{ws}^2}\left(\sigma - \frac{\sigma_s}{4\beta}\text{In}\cosh\frac{2\beta\sigma}{\sigma_s}\right) - \frac{4\theta\lambda_s\sigma\left(M^3 - M_r^3(\sigma)\right)}{\mu_0 M_\mathrm{ws}^4}, \sigma < 0 \end{cases} \tag{4}$$

$$M_r(\sigma) = \begin{cases} M_\mathrm{ws}(1 - tanh(\beta\sigma/\sigma_s)), \sigma \geq 0 \\ M_\mathrm{ws}(1 - tanh(2\beta\sigma/\sigma_s)/2), \sigma < 0 \end{cases} \tag{5}$$

$$M_\mathrm{an} = M_s\left(coth\left(\frac{H_e}{a}\right) - \frac{a}{H_e}\right) \tag{6}$$

where H_e is the effective magnetic field with applied stress, H_0 is the external magnetic field, which can be regarded as the geomagnetic field without an applied magnetic field, a and β are the shape coefficients, λ_s is the saturated magnetostrictive strain, M_ws is the magnetization as the domain wall motion process is completed without stress, σ_s is the stress when the magnetostrictive strain is saturated, $M_r(\sigma)$ is the transition point of M_ws denoting the saturation magnetization associated with the domain wall motion under a given stress σ, and θ is the step function. When $M \geq M_r(\sigma)$, $\theta = 3/4$, the magnetization increases monotonically, and when $M < M_r(\sigma)$, θ=0, the magnetic domain rotation causes the magnetization to decrease. M_{an} is the anhysteretic magnetization, M_s is the saturation magnetization, and α is the coefficient that characterizes the binding ability of the magnetic moment to the magnetization.

By solving Eqs. (4), (5) and (6), M_{an} of the ribbed steel bar under the stress and external magnetic field under ideal magnetization conditions can be obtained.

2.2.Magneto-mechanical model during fatigue

According to the description of the approach law proposed by Jilse [14], the M of ferromagnetic material tends to be M_{an} during magnetization under cyclic loads, as shown in Eq. (7). However, due to the accumulation of fatigue damage in the material, magnetic domain wall pinning acts as an obstacle during magnetization, and the material cannot be ideally magnetized to M_{an}. From the perspective of a macro energy balance, Xu et al. [20] assumed that the magnetization state under an energy loss caused by pinning is the local equilibrium magnetization M_0, considered that the M in the fatigue continues to approach the M_0, and modified the J-A-S model. The local equilibrium magnetization considering the pinning effect is shown in Eq. (8), which means that M_0 will continuously overcome pinning obstacles under cyclic loads and finally reach M_{an}.

$$\frac{dM}{d\sigma} = \frac{\sigma}{\xi E}(M_{\text{an}} - M) + c\frac{dM_{\text{an}}}{d\sigma} \tag{7}$$

where E is the Young's modulus, ξ is a parameter related to the energy density, and c is a parameter describing the flexibility of domain wall motion.

$$\frac{dM_0}{d\sigma} = \frac{\sigma}{AEk}(M_{\text{an}} - M_0) \tag{8}$$

where A is a parameter determined by the test results, k is the domain wall pinning coefficient, $k = n\langle\varepsilon_\pi\rangle/(2m)$, n is the density of the pinning, $\langle\varepsilon_\pi\rangle$ is the 180° domain wall pinning average energy,

$\langle \varepsilon_\pi \rangle \propto 2m\mu_0 H_e$, and m is the magnetic moment per unit volume [26].

Dislocations are defects caused by the local irregular arrangement of atoms in the material, which can hinder pinning of the motion of domain walls. The pinning point in the material that blocks the movement of the domain wall increases with an increasing dislocation. It is assumed that the pinning point density is proportional to the dislocation density, as follows [27]:

$$n \propto (n_0 + l) \tag{9}$$

where n_0 is the pinning point density caused by the initial defect of the crystal and l is the plugging dislocation density.

Dislocation will move inside the material under cyclic loading. According to the dislocation plugging theory, the density of dislocations per unit volume, regardless of temperature, can be expressed as:

$$l = \rho b \bar{\lambda} \tag{10}$$

where ρ is the dislocation density, b is the Berkeley vector magnitude of the dislocation, and $\bar{\lambda}$ is the average dislocation slip distance.

Substituting Eqs. (8) and (9) into $k = n\langle \varepsilon_\pi \rangle/(2m)$, the relationship between the domain wall pinning coefficient and the dislocations is as follows:

$$k \propto \mu_0 \left(n_0 + b\rho\bar{\lambda}\right) H_e \tag{11}$$

Referring to the Gilman relationship [28], there is a quantitative relationship between the shear plastic strain and dislocation, $\gamma_p = \rho b \bar{\lambda}$. Since the shear plastic strain is linearly related to the axial plastic strain, Eq. (11) is substituted into Eq. (8) in order to obtain the expression of the local equilibrium magnetization related to the plastic strain:

$$\frac{dM_0}{d\sigma} = \frac{\sigma(M_{\mathrm{an}} - M_0)}{A\mu_0 H_e E\left(n_0 + \varepsilon_p\right)} \tag{12}$$

In the fatigue, M constantly tends to M_0 instead of M_{an}, modifying the approach law described in Eq. (7) proposed by Jiles, the magnetization of ferromagnetic materials satisfies the following equation.

$$\frac{dM}{d\sigma} = \frac{\sigma}{\xi E}(M_0 - M) + c\frac{dM_0}{d\sigma} \tag{13}$$

Substituting M_{an} into Eq. (12), and solving Eqs. (12) and (13) simultaneously by the ODE function in the commercial software MATLAB, M can be calculated in each cycle.

3. Tensile fatigue test of HRB400 ribbed steel bars

Both the mechanical and magnetization properties of ribbed steel bars are affected by the composition, processing technology and geometric size. To verify the proposed model, HRB400 ribbed steel bars, which are widely used in the construction of RC structures in China, were used in tensile fatigue tests. The mechanical and magnetic data of the specimens during the fatigue tests were measured and recorded in real time.

3.1.Specimen preparation

The length and nominal diameter of the HRB400 ribbed steel bar used in the test are 400 mm and 14 mm, respectively, and the local geometric dimensions of the specimen are shown in Fig. 1(a). The chemical composition and mechanical properties of the material are shown in Table 1 and Table 2. To avoid test failure caused by fracture at the clamping end due to the stress concentration, two protective aluminum layers with a thickness of 0.3 mm were wrapped at both ends of the specimen to reduce the stress concentration, as shown in Fig. 1(b).

Table 1. Chemical composition of the HRB400 ribbed steel bar. (wt%)

Element	C	Fe	Mn	Si	S	P	V
Wt	0.19	97.8	1.34	0.53	0.014	0.028	0.040

Table 2. Mechanical properties of the HRB400 ribbed steel bar.

Material	Young's modulus E/GPa	Yield Strength σ_y/MPa	Ultimate strength σ_u/MPa	Elongation δ/%
HRB400	207.29	425.17	581.20	25.77

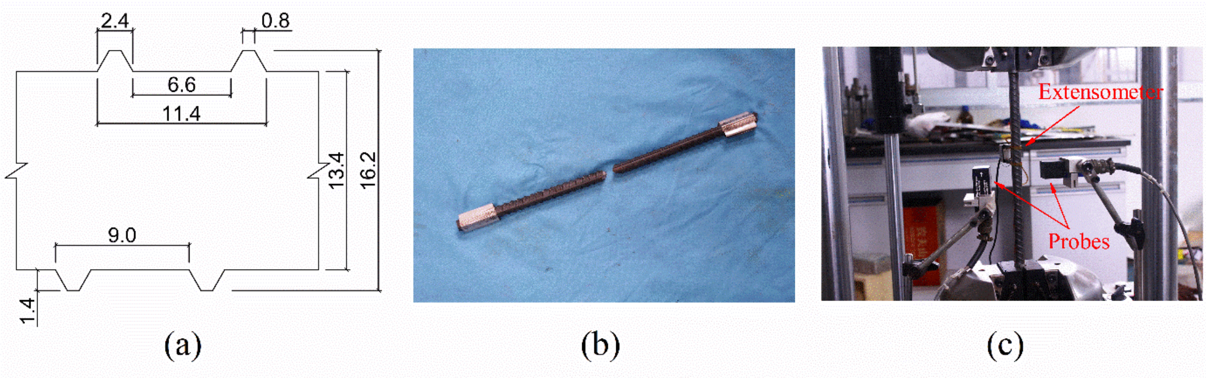

Fig. 1. Details of the specimen and sensors: (a) geometry of the specimen (mm); (b) protective layers of the clamping end; (c) specimen and sensor installations.

3.2.Loading and measurement

An electrohydraulic servo-controlled fatigue testing machine performed tests with a peak capacity of 250 kN for sinusoidal wave loading at a loading frequency of 2 Hz. A CRIMS extensometer with a range of 20 mm was used to measure the strain. Two APS 428D fluxgate magnetometers were placed in the middle of the specimen, 33 mm away from the specimen's surface, to measure the normal magnetic induction and tangential magnetic induction with a range of 1G and accuracy of ± 0.1%, respectively. A CRONOS Compact 400-08 dynamic data acquisition instrument with a sampling frequency of 1000 Hz was used for the synchronous data acquisition of stress, strain and magnetic induction intensity. Due to the great difference of magnetization properties and the fluctuation of environmental magnetic field, the magnetic signal of the specimens was zeroed out before the test. The test device installations and the loading parameters are shown in Fig. 1(c) and Table 3, respectively.

Table 3. Parameters and results of the fatigue test.

Number	S_{min}	S_{max}	$\Delta\sigma$	N_f
TFB1	0.1	0.60	290.60	353586
TFB2	0.1	0.60	290.60	283553
TFB3	0.1	0.60	290.60	282566
TFB4	0.1	0.65	319.66	177239
TFB5	0.1	0.65	319.66	246789
TFB6	0.1	0.65	319.66	236897
TFB7	0.1	0.65	319.66	273019
TFB8	0.1	0.65	319.66	232575
TFB9	0.1	0.70	348.72	145077
TFB10	0.1	0.70	348.72	143913

Note: $S_{min} = \sigma_{min}/\sigma_u$, $S_{max} = \sigma_{max}/\sigma_u$, $\Delta\sigma = \sigma_{max} - \sigma_{min}$, and σ_u is the ultimate strength.

4. Analysis and discussion of the results

The failure mode of all specimens is fatigue fracture near the middle position. Table 3 shows the fatigue life N_f of each specimen. Due to the displacement of the specimen during the loading process, the relative position of the measuring point and the magnetic probe changed continuously, which will affect the measured magnetic induction intensity. The test results show that the disturbance amplitude of the normal magnetic induction is much smaller than that of the tangential magnetic induction, and the test results of normal magnetic induction have more obvious regularity. Therefore, the normal magnetic induction intensity B_n is mainly used for the following experimental analysis. The B_n of each specimen versus the number of loading cycles N is displayed in Fig. 2. Despite the differences in the loading ranges, the B_n of all specimens presented similar and systematic trends. At the initial stage, the B_n of each specimen rose rapidly and tended to a stable value. In the first half of the middle stage, the B_n of each specimen showed a steady increase, but the increase rate was very slow. In the second half of the middle stage, the B_n of some specimens dropped slightly, such as TFB1, 3, 5, 6, and 8. At the end of fatigue, the B_n of each specimen gradually accelerated, especially near fatigue fracture, where B_n varied dramatically. The B_n of the specimens at this stage may increase or decrease, except for the B_n of TFB2 and TFB10, which significantly increased. The B_n of remaining other specimens were reduced at the end of fatigue, and the reason for the difference in the variation trend of specimens in the second half of the middle stage and last stage will be mentioned in the following analysis. In addition, although the mechanical properties of ribbed bars are similar, their magnetic properties are totally different, the magnitudes of the magnetic signal of these specimens are very discrete. It is necessary to propose a reasonable evaluation method to characterize the relationship between magnetic signal and fatigue, which will be discussed in the simulation section.

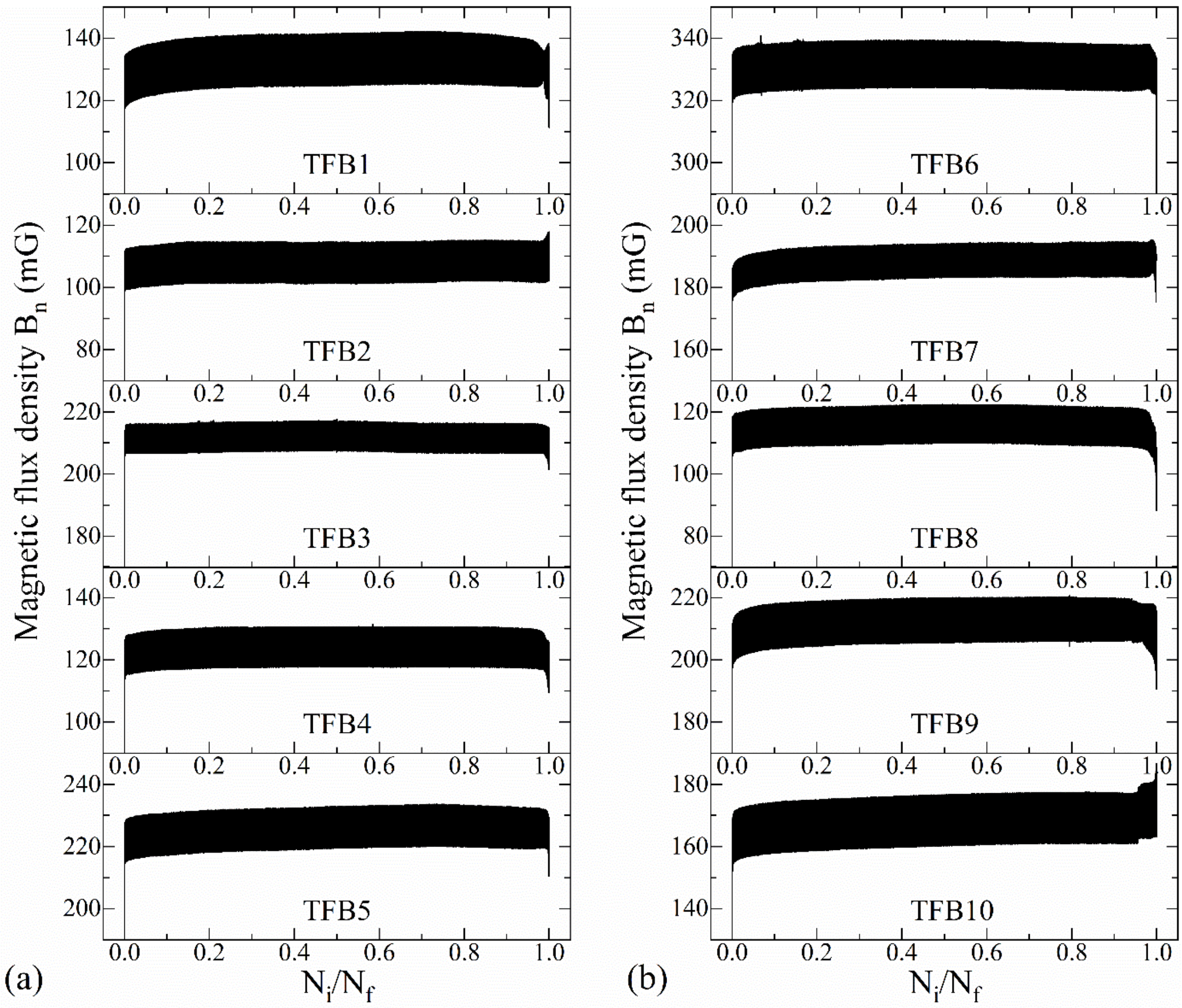

Fig. 2. Magnetic induction intensity curve in the fatigue test: (a) TFB1-5; (b) TFB6-10.

To analyze the characteristics of the magnetic signal more specifically, specimen TFB7 was taken as a typical example. The B_n and strain ε of the specimen versus cycle N are given in Fig. 3. It can be seen from the figure that B_n and ε show similar development trends. At the early stage of fatigue, both of them rapidly reached a stable value. Subsequently, their growth velocity began to decline but changed significantly before fatigue rupture.

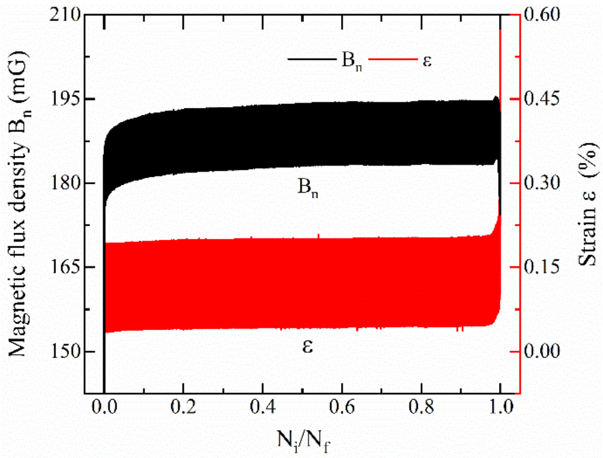

Fig. 3. Magnetic induction intensity curve and the strain curve of TFB7.

Fig. 4(a-b) displays the magnetic hysteresis curve of TFB7 in cycles 1-3. From Fig. 4(a), it can be observed that the specimen left an obvious remanence with 176.0 mG when it was unloaded to σ_{min} for the first time, indicating that the B_n of the specimen is very sensitive to the loading history. The magnetic hysteresis curve in cycles 2-3 is given in Fig. 4(b). Analyzing the difference value of B_n at the unloading point between adjacent cycles, $\triangle B_1$, $\triangle B_2$ and $\triangle B_3$ are 118.8 mG, 0.9 mG and 0.4 mG, respectively, in the first three cycles, and it can be determined that the growth rate of B_n decreases as the number of cycles increases. The same trend is also applicable to the early and middle stages of fatigue. The four characteristic hysteresis curves for cycles 10000-40000 in the early stage of fatigue are shown in Fig. 4(c). The values of B_n at the unloading point in each cycle are 183.6 mG, 184.6 mG, 185.5 mG and 185.8 mG, and the corresponding growths are 1 mG, 0.9 mG and 0.3 mG, respectively. Similarly, Fig. 4(d) gives the other four characteristic hysteresis curves for cycles 50000-200000 in the middle of fatigue. The values of B_n at the unloading point in each cycle are 186.1 mG, 187.0 mG, 187.7 mG and 188.1 mG, respectively. The average growth rate of B_n is approximately 0.18 mG, 0.14 mG and 0.08 mG every 10000 cycles. Compared with the early stage of fatigue, the growth rate of B_n was still declining until the last stage of fatigue. From the five characteristic hysteresis curves for cycles 250000, 270000 and 273017-273019 at the end of fatigue shown in Fig. 4(e), it can be observed that both the geometry and magnitude of the magnetic hysteresis curves obviously varied, and the shape of the curves gradually changed from full to narrow and no longer closed. At the same time, the change rate of B_n increased rapidly, and the value of B_n at the unloading point decreased from 175.6 mG to 174.0 mG and finally decreased to 29.9 mG before fatigue fracture.

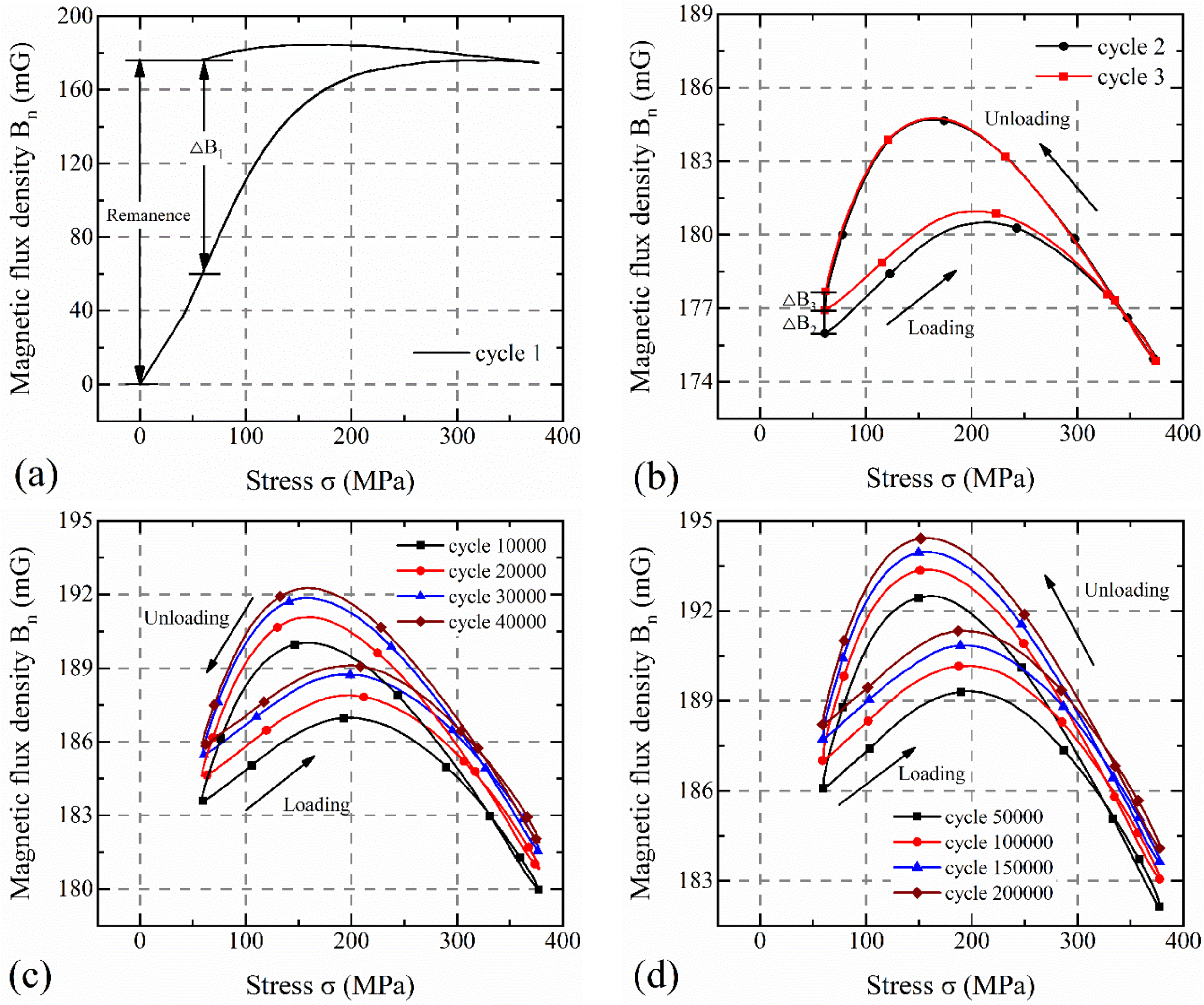

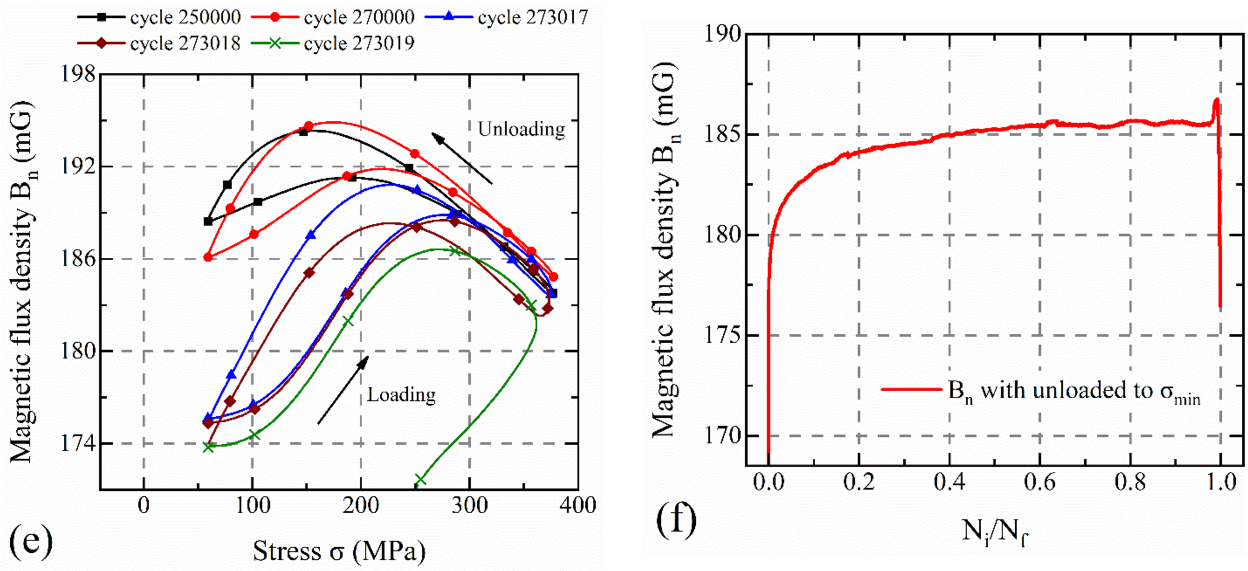

Fig. 4. Magnetic hysteresis loops of TFB7 during fatigue: (a) magnetic hysteresis loops for cycle 1; (b) magnetic hysteresis loops for cycles 2-3; (c) magnetic hysteresis loops for cycles 10000, 20000, 30000 and 40000; (d) magnetic hysteresis loops for cycles 50000, 100000, 150000 and 200000; (e) magnetic hysteresis loops for cycles 250000, 270000 and 273017-273019; (f) B_{n} unloaded to σ_{min} in each cycle.

To facilitate the analysis of the variation trend of B_{n}, take B_{n} unloaded to σ_{min} in each cycle as the characteristic point to obtain the B_{n} curve during fatigue, as shown in Fig. 4(f). The reasons for the change in B_{n} will be analyzed in detail with the proposed model and the microscopic mechanism. Before the specimen was loaded, the initial dislocation density was relatively low. This is because the crystal grains of the material were intact, and the internal defects and cracks mainly came from the production and processing processes. In the early stage of fatigue, due to the quick growth of the plastic strain, the dislocation within the material increased rapidly to a stable state, and microcracks began to initiate during this process [29]. In the middle stage of fatigue, the plastic strain grew slightly. Since the dislocations reached a steady saturated state, the dislocation density also did not increase obviously. However, the dislocation structure began to change significantly, and the slip band formed and gradually stabilized [30]. As the fatigue progresses, accompanied by the formation and increase in the primary and secondary slip bands, microcracks continue to develop. It can be seen from Eq. (11)

that the domain wall pinning and dislocations are proportional, and the dislocations of the specimens grow rapidly in the early fatigue stage. According to the magnetic domain wall pinning effect, the motion of the magnetic domains will be blocked by pinning. As a result, the growth rate of B_n dropped rapidly in the early fatigue stage. In the middle fatigue stage, the dislocations were in a stable state and changed slowly, so that the influence of domain wall pinning on the magnetization also showed a stable trend, which made B_n stable and varied slightly in the middle of the fatigue.

At the end of fatigue, the B_n of the specimen changed considerably, mainly affected by the leakage magnetic field at the cracks caused by fatigue damage. The direction and strength of these leakage magnetic fields are related to the location and size of the cracks. The dislocation density at this stage did not vary much, but the dislocation structure changed significantly. The microcracks grew and merged with dislocation slipping and aggregation, leading to the formation and propagation of macroscopic cracks [31], which means that with the development of cracks in the last stage of fatigue, the influence of the magnetic flux leakage on B_n became more significant, and the magnetic leakage effect played a leading role in the variation in B_n. Fig. 5 gives a schematic diagram of the magnetic field composition of the specimen. The magnetic field around the specimen is mainly composed of an environmental magnetic field H_0 and a magnetic field H_S caused by stress and a leakage magnetic field H_L at the crack. In the early stage and the first half of the middle stage, under the geomagnetic field and cyclic loads, the internal magnetization M of the material changed under the influence of dislocation magnetization, which caused the magnetic field H_S to change. At the end of fatigue, due to the continuous expansion of cracks caused by fatigue damage, many macroscopic cracks occurred inside and on the surface of the material. Magnetic charges accumulated at the cracks and generated leakage magnetic fields H_L. These leakage magnetic fields caused sudden changes in the local magnetic field at the cracks, which led to abrupt variations in B_n in the last fatigue stage. On the other hand, the B_n measured in the test is affected by the measurement position, magnetization properties of the material, crack position and geometric dimension. The dispersion of the magnetization properties and the randomness of the crack location and size caused B_n to increase or decrease in the last fatigue stage. In addition, due to the ribs, the specimens have stress concentrations, which accelerate the development of fatigue cracks. Some specimens were affected by the leakage field at cracks in the second half of the middle stage, so B_n did not increase steadily, but rather decreased slightly.

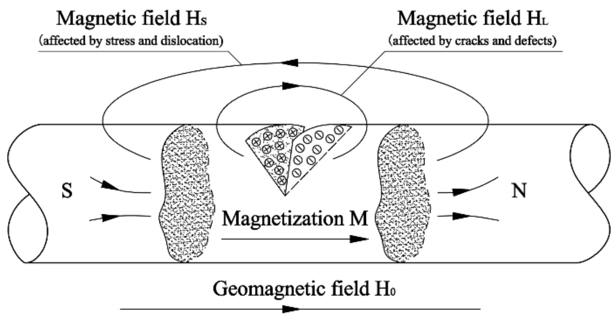

Fig. 5. Magnetic field schematic diagram of the specimen at the end of fatigue.

5. Equivalent local stress and fatigue life considering stress concentration

Due to the stress concentration caused by ribs, not only will the fatigue life of ribbed steel bars be reduced but the actual stress will also be changed, which affects the magnetic signal. The equivalent local stress and fatigue life of ribbed steel bars under a nominal cyclic stress will be determined by the Neuber law and the Coffin-Manson relation.

5.1.Equivalent local stress and strain

The constitutive curve of ribbed steel bars under cyclic loading can be described by the Ramberg-Osgood (R-O) model [32].

$$\varepsilon = \frac{\sigma}{E} + \left(\frac{\sigma}{k'}\right)^{\frac{1}{n'}} \quad (14)$$

where σ is the stress, ε is the strain, E is Young's modulus, and k' and n' are the cyclic strain hardening coefficient and exponent, respectively.

Because the stress concentration mainly occurs in the ribs and its influence range is relatively small, the overall constitutive relationship of ribbed steel bars still satisfies the R-O model, while the stress and strain in the local area affected by the stress concentration are higher than the nominal stress and strain, respectively. There are currently many methods that can be used to determine the local stress and strain of ribbed steel bars, among which the Neuber law is most widely used, as shown in Eq. (15) [33]. By introducing the stress concentration coefficient, the nominal stress and strain are correlated with the equivalent local stress and strain. Substituting the maximum nominal stress σ_{max}^{N} and the minimum nominal stress σ_{min}^{N} into Eqs. (14) and (15), the equivalent local stress and strain can be obtained (σ_{max}^{L}, σ_{min}^{L}, ε_{max}^{L}, ε_{min}^{L}). Fig. 6 gives the specific relation diagram, in which the Neuber equation can be approximated by a hyperbola, and the intersection point of the Neuber equation and the R-O model is the equivalent local $\sigma - \varepsilon$ point.

$$\sigma^{L}\varepsilon^{L} = \left(K_f\sigma^{N}\right)^2/E \tag{15}$$

where σ^{L} is the equivalent local stress, ε^{L} is the equivalent local strain, σ^{N} is the nominal stress, and K_f is the fatigue notch coefficient, which is affected by the notch geometry and material. Elrefai et al. [34] believe that the K_f in RC beams under cyclic loading can be set at 2.0. Badawi et al. [35] suggested that K_f could be set at 2.0 with a short fatigue life and 2.1 with a long fatigue life through fatigue tests of RC beams.

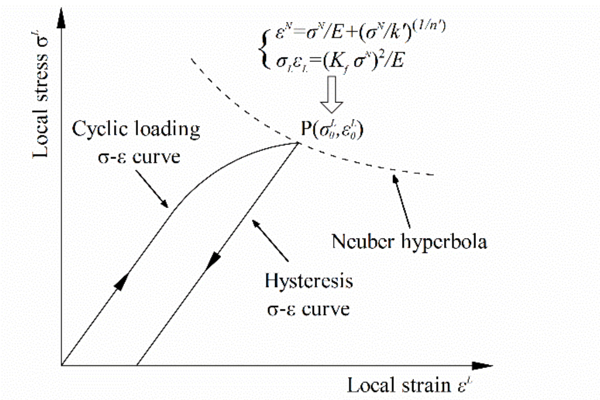

Fig. 6. The intersection of the Neuber hyperbola and the cyclic stress-strain curve.

5.2.Fatigue life of ribbed steel bars

Ribbed steel bar fatigue fracture usually occurs in the rib, and the fatigue life is largely influenced by the local stress and strain of the rib area. Based on the periodic $\sigma - \varepsilon$ behavior of the bars, the massing hypothesis can be used to determine the stable $\sigma - \varepsilon$ hysteresis curve, and the local stress range $\Delta\sigma^L$ and strain range $\Delta\varepsilon^L$ can be obtained by substituting the nominal stress range $\Delta\sigma^N = \sigma_{max}^N - \sigma_{min}^N$ into Eqs. (16) and (17).

$$\Delta\varepsilon^L = \frac{\Delta\sigma^L}{E} + 2\left(\frac{\Delta\sigma^L}{2k'}\right)^{\frac{1}{n'}} \quad (16)$$

$$\Delta\sigma^L \Delta\varepsilon^L = \left(K_f \Delta\sigma^N\right)^2 / E \quad (17)$$

The Coffin-Manson relationship can be used to express the relationship between the strain range and fatigue life, as given in Eq. (18) [36, 37]. The local strain range $\Delta\sigma^L$ can be obtained by the Neuber law mentioned above, and the coefficients σ_f', ε_f', b and c are usually determined by fatigue tests on smooth specimens processed by ribbed steel bars. Jin et al. [38] performed a fatigue test on smooth specimens processed with HRB400 steel bars and obtained $\sigma_f' = 1368.01$ MPa, $\varepsilon_f' = 0.313$, $b = -0.124$, and $c = -0.485$. In addition, the coefficients k' and n' in the RO model can be approximated by the parameters of the Coffin-Manson relationship [39], where $n' = b/c$, $k' = \sigma_f' / (\varepsilon_f'^{\,n'})$. Through the Neuber law and the Coffin-Manson relationship, the fatigue life of specimens under different nominal stress ranges $\Delta\sigma^N$ and the fatigue notch coefficients K_f can be obtained, as shown in Fig. 7. It can be determined that the calculation results are closer to the test results with $K_f = 2.05$, so the following numerical simulation analysis will take $K_f = 2.05$.

$$\frac{\Delta\varepsilon^L}{2} = \frac{\sigma_f'}{E_s}(2N_f)^b + \varepsilon_f'(2N_f)^c \quad (18)$$

where σ_f' is the fatigue strength coefficient, ε_f' is the fatigue ductility coefficient, b is the fatigue strength index, c is the fatigue ductility index, and N_f is the fatigue life.

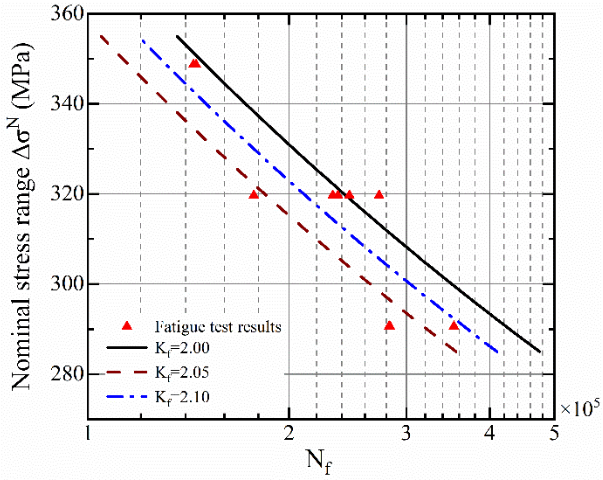

Fig. 7. Stress range versus fatigue life of the ribbed steel bars.

6. Numerical simulation and analysis

6.1.Determining the residual plastic strain of ribbed steel bars

According to Eqs. (11) and (12), it can be seen that the magnetization state of ribbed steel bars is affected by domain wall pinning, which can be characterized by plastic strain. Under cyclic loads, the domain wall pinning will vary constantly, which is difficult to simulate and analyze. To facilitate the simulation, the domain wall pinning coefficient k of each cycle is taken as a fixed value, which is calculated by the accumulated residual strain ε_p in each cycle. Since the variation trend of the magnetization in the proposed model is mainly affected by the development trend of plastic strain, the fitting formula of residual strain that satisfies the three-stage fatigue development trend given by Ouyang et al. [40] in the tensile fatigue test of ribbed steel bars is used to fit the test data. The fitting results of the plastic strain of the specimens with different loading levels are shown in Fig. 8. Since the stress at the unloading point of the test is $0.1\sigma_u$, the cumulative residual strain is taken as $\varepsilon_p(n)=\varepsilon_{min} - 0.1\sigma_u/E$.

$$\varepsilon_p(n)=k_1\left(\frac{1}{1-\frac{n}{N_f}}-1\right)^{\frac{1}{k_2}} \tag{20}$$

where $\varepsilon_p(n)$ is the cumulative plastic strain after n cycles and k_1 and k_2 are the fitting coefficients.

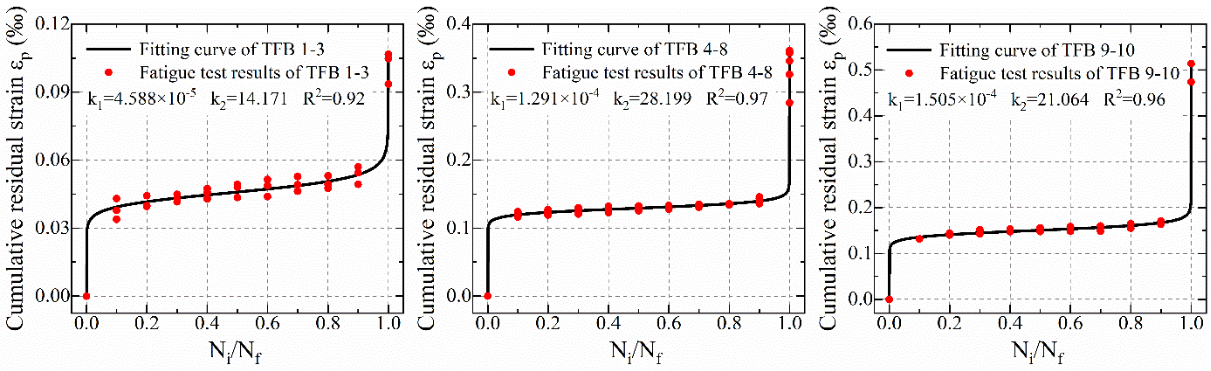

Fig. 8. Cumulative residual strain fitting curve of the specimens.

6.2.Numerical simulation of the magnetization of ribbed steel bars

Because the magnetization performance of specimens is mainly affected by the material, partial parameters of the simulation are determined by the existing references to make the simulation results more reliable. The geomagnetic field H_0 can be considered as 40 A/m. The main component of the ribbed steel bars is mild steel, which can be regarded as a soft ferromagnetic material rod. Zhou et al. [25] and Shi et al. [22] gave the simulation parameters of the soft ferromagnetic material rod, $N_d = 1.0 \times 10^{-3}$, $\lambda_s = 4.17 \times 10^{-6}$, $M_s = 1.5 \times 10^6$A/m, $M_{ws} = 1.0 \times 10^6$A/m, and $\beta = 1.5$. The simulation parameters of mild steel given by Jiles et al. [13] are $\alpha = 1.1 \times 10^{-3}$, $\xi = 605$, $a = 0.9 \times 10^3$, $c = 0.1$. The remaining parameters are taken from the simulation results of Huang et al. [23] on smooth specimens processed by HRB400 steel bars, $\sigma_s = 400$ MPa, $A = 1.0 \times 10^{10}$, and $n_0 = 1.0 \times 10^{-4}$. Substituting the equivalent local stresses σ_{max}^L and σ_{min}^L obtained by the Neuber law, the fatigue life N_f obtained from the Coffin-Manson relationship, and the cumulative residual strain $\varepsilon_p(n)$ of each cycle obtained by fitting into the proposed model, the magnetization M of the specimen in each cycle can be calculated. The magnetization analysis process of ribbed steel bar under cyclic loading is shown in Fig. 9.

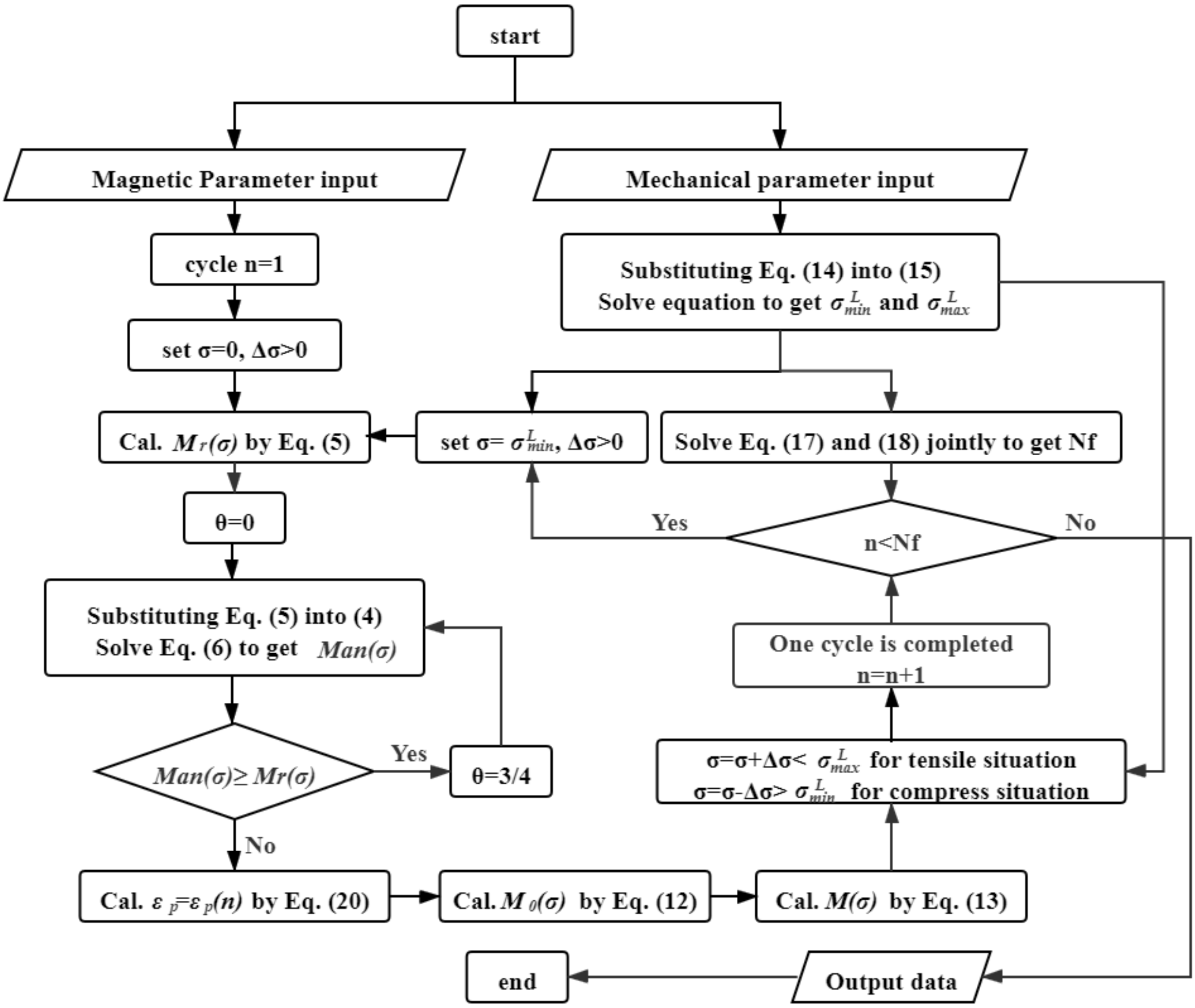

Fig. 9. The magnetization analysis process of ribbed steel bar under cyclic loading.

The simulation results M and the test results B_n unloaded to the minimum stress point in each cycle are shown in Fig. 10. It can be observed that the development trends of the test curve and the simulation curve are similar in the early and middle stages of fatigue. B_n increased rapidly in the early stage, and the growth rate of B_n continued to decrease until fatigue failure, which satisfies the description of the approach law. However, the change trends of the simulation curve and the test curve are quite different. The reason is that the proposed model only considers the magneto-mechanical effects in fatigue. At the end of fatigue, the magnetic flux leakage effect played a leading role in B_n, which caused the magnetic induction intensity at the measuring point to decrease at this stage and drop dramatically before the fracture. According to the proposed model, M will continuously approach M_0 during fatigue. It can be seen from Eq. (13) that the change in magnetization with stress $\mathrm{d}M/\mathrm{d}\sigma$ is related to the value of $M_0 - M$. Because the specimen was not stressed before loading, the difference between M_0 and M was large. In the early stage of fatigue, the M of the specimen quickly approached M_0. In the subsequent fatigue process, M gradually reached M_0, and the value of $M_0 - M$ declined, resulting in a decrease in the growth rate of M. In addition, the magnitude of M is very different from that of B_n measured by the test. The main reason is that the simulation is the internal magnetization of the material, the magnetic induction measured by the test is affected by the measurement position, and its magnitude will be much smaller than the internal magnetization of the material.

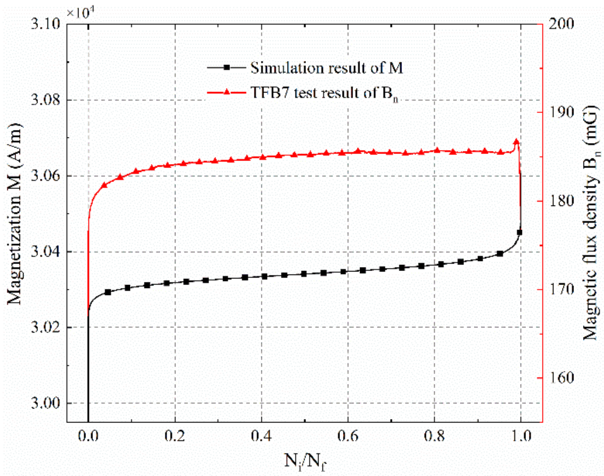

Fig. 10. Magnetic flux density from the experiment and magnetization from the numerical simulation of TFB7.

6.3.Fatigue damage formula of the magnetic indicators

To reduce the influence of the magnetic flux leakage effect on the magnetic induction intensity of specimens, the following analysis focuses on the first two stages of fatigue ($0 < N \leq 0.85N_f$), where the magnetic leakage effect has a relatively small influence. At the same time, to eliminate the magnitude difference between the simulated magnetization M and the measured magnetic induction intensity B_{n}, the fatigue damage formula based on the magnetic indicators [4] is introduced to verify the accuracy of the proposed model. Considering that the B_{n} of some specimens in the middle and final stages slightly decreased (TFB1, 3, 5, 6, and 8), the decreased part of B_{n} still reflected the fatigue damage, and the absolute value of the B_{n} variation was taken to calculate the fatigue damage.

$$D_B(N) = \frac{\sum_{i=1}^{N}|\triangle B_i|}{\sum_{i=1}^{0.85N_{\mathrm{f}}}|\triangle B_i|} \qquad (19)$$

where $\triangle B_i = B(i) - B(i-1)$ is the difference in B_{n} at the characteristic points of cycle i and cycle $i-1$, and $\sum_{i=1}^{N}|\triangle B_i|$ and $\sum_{i=1}^{0.85N_{\mathrm{f}}}|\triangle B_i|$ are the cumulative absolute values of the B_{n} variation in cycles $1-N$ $(1 \leq N \leq 0.85N_f)$ and cycles $1-0.85N_{\mathrm{f}}$, respectively.

The fatigue damage curve with the simulation and test data of TFB7 calculated by Eq. (19) are shown in Fig. 11. The two curves have similar variation trends, showing nonlinear rapid growth in the early stage of fatigue and an almost linear growth in the middle stage of fatigue. The simulated fatigue damage curve, which is slightly higher than the test curve overall, shows that the simulated results are more conservative than the test results. The fatigue damage comparison results of the remaining specimens also reflect the same law. Fig. 12(a-c) shows the fatigue damage curve under the three sets of loading levels. In addition to the above rules, for specimens TFB1, 3, 5, 6, and 8, whose B_{n} decreased slightly in the second half of the middle stage, it can be determined from the partially enlarged curve that the slight decrease in B_{n} caused the fatigue damage curve to produce a slope turning point. After the turning point, the slope of the fatigue damage curve increases, and fatigue damage develops more rapidly. It has been explained above that the decrease in B_{n} may be caused by the leakage field at the fatigue crack. The accelerated development of the fatigue damage caused by fatigue cracks will also be reflected in the measured magnetic signal, which proves the high sensitivity of the magnetic signal to microscopic damage.

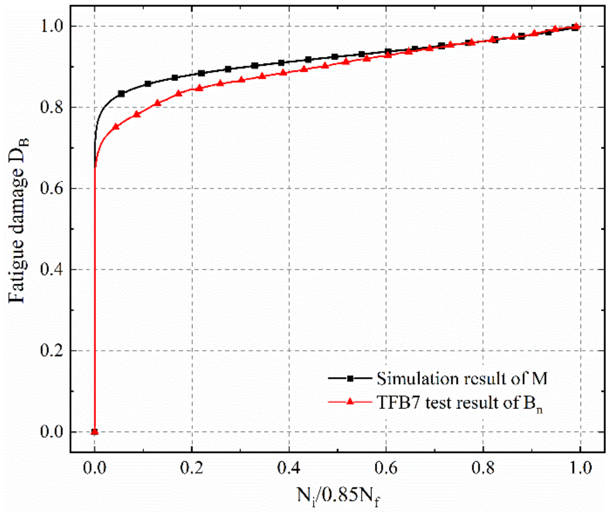

Fig. 11. Fatigue damage curves based on experimental data and simulated results of TFB7.

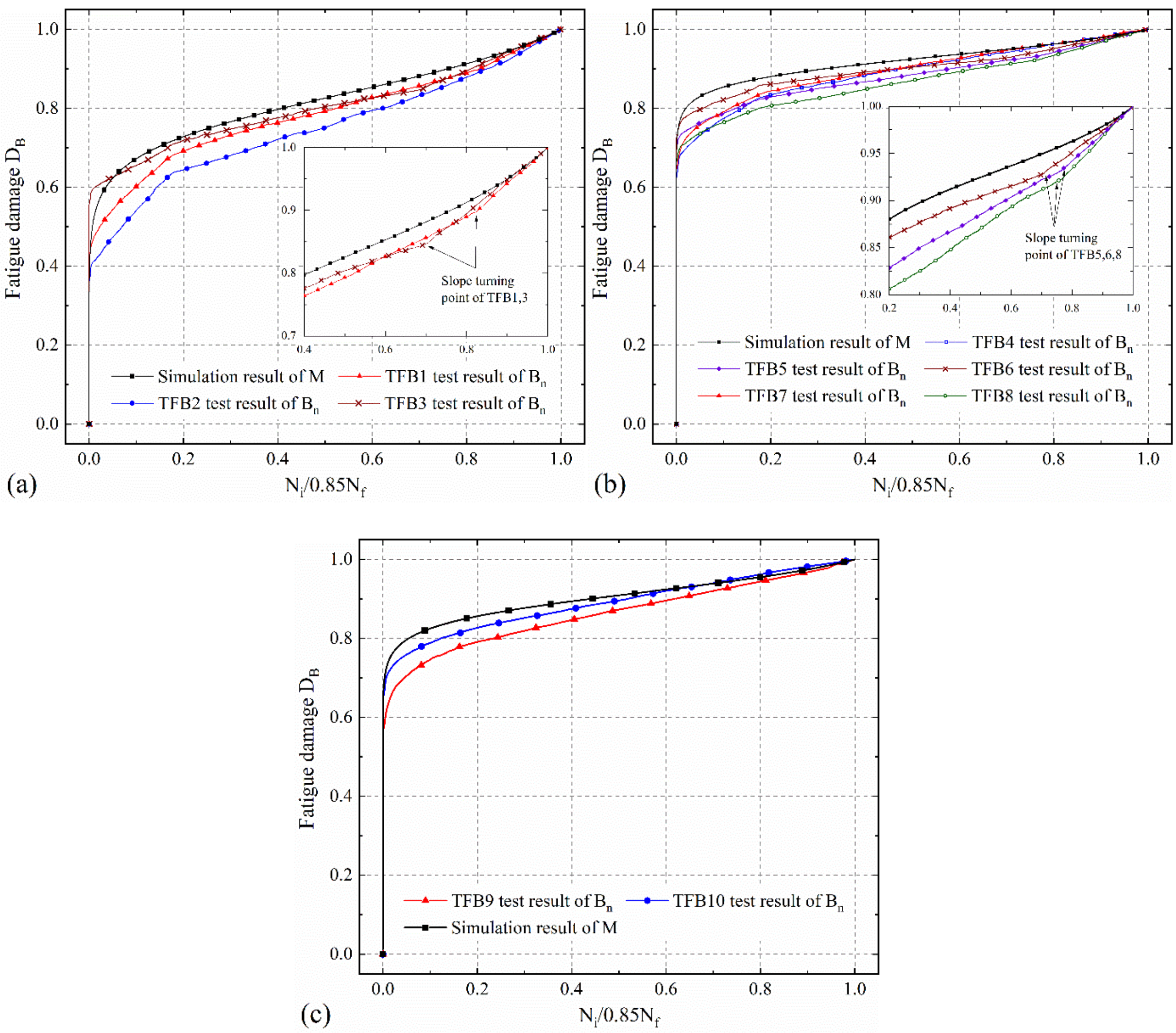

Fig. 12. Fatigue damage curves based on experimental data and simulated results: (a) TFB1-3; (b) TFB4-8; (c) TFB9-10.

7. Conclusion

Considering the influence of the stress concentration at the ribs of steel bars, the equivalent stress and the fatigue life of the ribbed steel bars were determined by the Neuber law and Coffin-Manson relationship, and a magneto-mechanical model of the ribbed steel bar was established to predict the magnetization during fatigue. In addition, the cumulative plastic strain fitting formula that reflects the three-stage fatigue trend was used so the simulation parameters would no longer depend on the measured test data. According to the magnetic induction intensity measured by the tensile fatigue test of the HRB400 ribbed steel bars, the relationship between the magnetic induction intensity and the fatigue damage was discussed from the perspective of micro-mechanisms. The magnetization of the specimen conforms to the description of the proposed model. When there is no macro crack, the growth rate of magnetization decreases continuously, which is mainly affected by pinning related to plastic deformation. And the growth trend of magnetic signal can be used to predict the macroscopic damage propagation. Comparing the test and simulation results calculated by the fatigue damage formula based on the magnetic indicator, the results showed that the proposed model could effectively describe the fatigue damage state of ribbed steel during fatigue, which verifies the applicability and accuracy of the model. These results are very helpful in understanding the magneto-mechanical behavior of ribbed steel bars in RC beams during fatigue, which is of great significance to fatigue damage monitoring in actual engineering.

Acknowledgments

The financial supports from the National Natural Science Foundation of China (Grant No. 51878604, 52078454, 51820105012, 51908496) are gratefully acknowledged.

References

1. Suresh S. *Fatigue of Materials*. Cambridge: Cambridge University Press, 1998.
2. Anonymous. Fatigue Testing and Analysis: Theory and Practice. *Mechanical Engineering*. New York: American Society of Mechanical Engineers, 2004, p. 59.
3. Shi P, Su S and Chen Z. Overview of Researches on the Nondestructive Testing Method of Metal Magnetic Memory: Status and Challenges. *Journal of Nondestructive Evaluation* 2020; 39: 43. DOI: 10.1007/s10921-020-00688-z.
4. Zhang J, Jin W, Mao J, et al. Determining the fatigue process in ribbed steel bars using piezomagnetism. *Construction and Building Materials* 2020; 239: 117885. DOI: https://doi.org/10.1016/j.conbuildmat.2019.117885.
5. Villari E. Change of magnetization by tension and by electric current. *Ann Phys Chem* 1865; 126: 87-122.
6. Erber T, Guralnick SA, Desai RD, et al. Piezomagnetism and fatigue. *Journal of Physics D: Applied Physics* 1997; 30: 2818-2836. DOI: 10.1088/0022-3727/30/20/008.
7. Guralnick SA, Bao S and Erber T. Piezomagnetism and fatigue: II. *Journal of Physics D: Applied Physics* 2008; 41: 115006. DOI: 10.1088/0022-3727/41/11/115006.
8. Bao S, Erber T, Guralnick SA, et al. Fatigue, Magnetic and Mechanical Hysteresis. *Strain* 2011; 47: 372-381. DOI: 10.1111/j.1475-1305.2010.00739.x.
9. Bao S and Gong SF. Magnetomechanical behavior for assessment of fatigue process in ferromagnetic steel. *Journal of Applied Physics* 2012; 112: 113902. DOI: 10.1063/1.4769364.
10. Bao S, Jin WL and Huang MF. Mechanical and magnetic hysteresis as indicators of the origin and inception of fatigue damage in steel. *Journal of Zhejiang University-Science A* 2010; 11: 580-586. DOI: 10.1631/jzus.A1000178.
11. Bao S, Jin WL, Huang MF, et al. Piezomagnetic hysteresis as a non-destructive measure of the metal fatigue process. *NDT and E International* 2010; 43: 706-712. DOI: 10.1016/j.ndteint.2010.08.002.
12. Xu M, Xu M, Li J, et al. In service detection of 45 steel's rotary bending fatigue damage based on metal magnetic memory technique. In: 2010 pp.4301-4304.
13. Jiles DC. Theory of the magnetomechanical effect. *Journal of Physics D: Applied Physics* 1995; 28: 1537-1546. DOI: 10.1088/0022-3727/28/8/001.
14. Jiles DC and Atherton DL. Theory of the magnetisation process in ferromagnets and its application to the magnetomechanical effect. *Journal of Physics D: Applied Physics* 1984; 17: 1265-1281. DOI: 10.1088/0022-3727/17/6/023.
15. Jiles DC and Devine MK. The law of approach as a means of modelling the magnetomechanical effect. *Journal of Magnetism and Magnetic Materials* 1995; 140-144: 1881-1882. DOI: 10.1016/0304-8853(94)00928-7.
16. Sablik MJ and Jiles DC. Coupled magnetoelastic theory of magnetic and magnetostrictive hysteresis. *IEEE Transactions on Magnetics* 1993; 29: 2113-2123. DOI: 10.1109/20.221036.
17. Sablik MJ, Kwun H, Burkhardt GL, et al. Model for the effect of tensile and compressive stress on ferromagnetic hysteresis. *Journal of Applied Physics* 1987; 61: 3799-3801. DOI: 10.1063/1.338650.
18. Sablik MJ and Landgraf FJG. Modeling microstructural effects on hysteresis loops with the same maximum flux density. *IEEE Transactions on Magnetics* 2003; 39: 2528-2530. DOI: 10.1109/TMAG.2003.816466.
19. Li J, Xu M, Leng J, et al. Modeling plastic deformation effect on magnetization in ferromagnetic materials. *Journal of Applied Physics* 2012; 111. DOI: 10.1063/1.3695460.

20. Xu MX, Xu MQ, Li JW, et al. Using Modified J-A model in MMM detection at elastic stress stage. *Nondestructive Testing and Evaluation* 2012; 27: 121-138. DOI: 10.1080/10589759.2011.622758.

21. Zheng XJ and Liu XE. A nonlinear constitutive model for Terfenol-D rods. *Journal of Applied Physics* 2005; 97: 053901-053901-053908. DOI: 10.1063/1.1850618.

22. Shi PP, Jin K and Zheng XJ. A magnetomechanical model for the magnetic memory method. *International Journal of Mechanical Sciences* 2017; 124-125: 229-241. DOI: 10.1016/j.ijmecsci.2017.03.001.

23. Zhang D, Huang W, Zhang J, et al. Theoretical and experimental investigation on the magnetomechanical effect of steel bars subjected to cyclic load. *Journal of Magnetism and Magnetic Materials* 2020; 514: 167129. DOI: https://doi.org/10.1016/j.jmmm.2020.167129.

24. Shi P, Jin K and Zheng X. A general nonlinear magnetomechanical model for ferromagnetic materials under a constant weak magnetic field. *Journal of Applied Physics* 2016; 119: 145103. DOI: 10.1063/1.4945766.

25. Zhou HM, Zhou YH and Zheng XJ. A general theoretical model of magnetostrictive constitutive relationships for soft ferromagnetic material rods. *Journal of Applied Physics* 2008; 104: 023907-023907-023909. DOI: 10.1063/1.2957075.

26. Jiles DC and Atherton DL. Theory of ferromagnetic hysteresis. *Journal of Magnetism and Magnetic Materials* 1986; 61: 48-60. DOI: https://doi.org/10.1016/0304-8853(86)90066-1.

27. Xu MX, Chen ZH, Xu MQ, et al. Discussion of modified Jiles-Atherton model including dislocations and plastic strain. *International Journal of Applied Electromagnetics and Mechanics* 2015; 47: 61-73. DOI: 10.3233/JAE-130159.

28. Gilman JJ. Dislocation Mobility in Crystals. *Journal of Applied Physics* 1965; 36: 3195-3206. DOI: 10.1063/1.1702950.

29. Xu MX, Chen ZH and Xu MQ. Micro-mechanism of metal magnetic memory signal variation during fatigue. *International Journal of Minerals Metallurgy and Materials* 2014; 21: 259-265. DOI: 10.1007/s12613-014-0903-z.

30. Grosskreutz JC. The mechanisms of metal fatigue (I). *physica status solidi (b)* 1971; 47: 11-31. DOI: 10.1002/pssb.2220470102.

31. Grosskreutz JG. The mechanisms of metal fatigue (II). *physica status solidi (b)* 1971; 47: 359-396. DOI: 10.1002/pssb.2220470202.

32. Heffernan PJ and Erki MA. Fatigue Behavior of Reinforced Concrete Beams Strengthened with Carbon Fiber Reinforced Plastic Laminates. *Journal of Composites for Construction* 2004; 8: 132-140. DOI: 10.1061/(ASCE)1090-0268(2004)8:2(132).

33. Neuber H. Theory of Stress Concentration for Shear-Strained Prismatical Bodies With Arbitrary Nonlinear Stress-Strain Law. *Journal of Applied Mechanics* 1961; 28: 544-550. DOI: 10.1115/1.3641780.

34. Elrefai A, West J and Soudki K. Fatigue of reinforced concrete beams strengthened with externally post-tensioned CFRP tendons. *Construction and Building Materials* 2012; 29: 246-256. DOI: https://doi.org/10.1016/j.conbuildmat.2011.10.014.

35. Badawi MA. Monotonic and Fatigue Flexural Behaviour of RC Beams Strengthened with Prestressed NSM CFRP Rods. UWSpace, 2007.

36. Coffin L. Study of the effect of cyclic thermal stresses on a ductile metal. *Trans ASME* 1954; 76.

37. Manson. Behavior of Materials Under Conditions of Thermal Stress. *Nat Advis Comm Aero Tech* 1953; 2933.

38. Jin L, Zeng B, Lu D, et al. Prediction of Strain Fatigue Life of HRB400 Steel Based on Meso-Deformation Inhomogeneity. *Materials* 2020; 13. DOI: 10.3390/ma13061464.

39. Li J, Zhang Z and Li C. An improved method for estimation of Ramberg–Osgood curves of steels from monotonic tensile properties. *Fatigue & Fracture of Engineering Materials & Structures* 2016; 39: 412-426. DOI: 10.1111/ffe.12366.
40. Xiang Sen O, Xiao Yong L and Jun W. The fatigue properties and damage of the corroded steel bars under the constant-amplitude fatigue load. *Journal of Vibroengineering* 2019; 21: 988-997. Article. DOI: 10.21595/jve.2018.20333.